

# Simulations of Spectral Polarimetric Variables measured in rain at W-band

Ioanna Tsikoudi<sup>1,2</sup>, Alessandro Battaglia<sup>3,4</sup>, Christine Unal<sup>5,6</sup>, and Eleni Marinou<sup>1</sup>

<sup>1</sup>Institute for Astronomy, Astrophysics, Space Applications and Remote Sensing, National Observatory of Athens, Greece

<sup>2</sup>Department of Physics, National and Kapodistrian University of Athens, Greece

<sup>3</sup>Department of Environment, Land and Infrastructure Engineering, Politecnico of Torino, Turin, Italy

<sup>4</sup>Department of Physics and Astronomy, University of Leicester, Leicester, UK

<sup>5</sup>Geoscience and Remote Sensing, Delft University of Technology, Netherlands

<sup>6</sup>Climate Institute, Delft University of Technology, Netherlands

**Correspondence:** jtsik@noa.gr

**Abstract.** In this work, the T-matrix approach is exploited to produce simulations of spectral polarimetric variables (spectral differential reflectivity,  $sZ_{DR}$ , spectral differential scattering phase,  $s\delta_{HV}$  and spectral correlation coefficient,  $s\rho_{HV}$ ) for observations of rain acquired from a slant-looking W-band cloud radar. The spectral polarimetric variables are simulated with two different methodologies, taking into account the instrument noise and the stochastic movement of the raindrops introduced by raindrop oscillations and by turbulence. The simulated results are then compared with rain Doppler spectra observations from a W band radar for moderate rain rate conditions. Two cases, differing in levels of turbulence, are considered. While the comparison of the simulations to the measurements presents a reasonable agreement for equi-volume diameters less than 2.25 mm, large discrepancies are found in the amplitude (but not the position) of the maxima and minima of  $sZ_{DR}$  and, more mildly, of  $s\delta_{HV}$ . This pinpoints at a general weakness of the raindrops approximation with spheroids for simulating radar backscattering properties at W-band.

## 1 Introduction

Cloud radar observations are crucial for understanding cloud microphysics, as proposed in the groundwork laid by radar pioneers (Atlas et al., 1973; Lhermitte, 1990). In the last 25 years this is corroborated by an abundance of studies based on vertically-pointing spectral Doppler cloud radar observations in multi-frequency configurations and/or in synergy with lidar and radiometers for better characterising drizzle (e.g. O'Connor et al., 2005; Kollias et al., 2011b; Luke and Kollias, 2013), rain (Kollias et al., 2001, 2002; Tridon et al., 2013; Tridon and Battaglia, 2015; Courtier et al., 2022), ice (Kalesse et al., 2016; Kneifel et al., 2016; Li et al., 2021; Luke et al., 2021), mixed-phase (Luke et al., 2010) and melting particles (e.g. Li and Moisseev, 2019; Mróz et al., 2021). Polarimetric variables provide additional constraints on hydrometeor shape and orientation and are routinely measured by ground-based precipitation radar networks using low-elevation scanning strategies (Chandrasekar et al., 2023 and reference therein). However, vertically pointing cloud radars miss most of the polarimetric information of hydrometeors (with the only exception of the linear depolarization ratio, (Mróz et al., 2021)), since hydrometeors

tend to fall with their maximum dimensions horizontally aligned. In order to overcome this limitation, more recently few sites started operating cloud radars with Doppler and polarimetric capabilities in slant observation mode (Myagkov et al., 2020; Unal and van den Brule, 2024; Mak and Unal, 2025). This configuration has the critical advantage that particles with  
25 different sizes are separated in the spectral domain (because they have different sedimentation velocities), which allows to disentangle the contributions of different particle types. While vertically pointing radars can also achieve this separation, radars in slant polarization mode additionally exploit polarimetric measurements. At higher frequencies like W-band, where multiple resonances occur across the particle size distribution (PSD), the polarimetric variables—resulting from integration over the entire PSD—tend to average out the characteristic features of single-particle scattering, often balancing positive  
30 and negative contributions ~~-.Consequently, these variables exhibit low-~~ (Kollias et al., 2011a). This is especially evident in the simulations of differential reflectivity ( $Z_{DR}$ ), where this parameter exhibits very low values and sensitivity to PSD variations (Unal and van den Brule, 2024). Further, ~~they~~ the polarimetric variables reflect both scattering and propagation effects. A way to mitigate these challenges at millimeter wavelengths is to analyze polarimetric variables in the spectral domain.

For Ka- and W-band observations of rain at a 45° elevation angle, Unal and van den Brule (2024) have demonstrated that  
35 using the Rayleigh plateau, as proposed in the literature (Tridon et al., 2013; Myagkov et al., 2020), allows for the separation of propagation and backscatter contributions in the spectral domain for polarimetric variables, specifically the differential phase shift and differential reflectivity. The differential phase at backscattering can then be utilized to infer the characteristic droplet diameter of the droplet size distribution (DSD). Incidentally W-band polarimetric radar observations at slant angles have been also proposed in the framework of the ESA spaceborne WIVERN mission (Illingworth et al., 2018; Battaglia et al., 2022),  
40 which aims to measure in-cloud winds by using the polarization diversity technique with an antenna conically scanning at an incidence angle of 41.6°. Although in WIVERN case no spectral measurements are envisaged, this mission will provide an unprecedented abundance of incidentally cloud radar polarimetric observations globally.

Spectral polarimetric observations, utilizing either slant or horizontal profiling, effectively distinguish hydrometeors from clutter (Bachmann and Zrnić, 2007; Moisseev and Chandrasekar, 2009; Unal, 2009; Chen et al., 2022) and also enable the  
45 characterization of various hydrometeors (Spek et al., 2008; Pfizenmaier et al., 2018; Wang et al., 2019; Lakshmi et al., 2024). In the case of rain, Moisseev et al. (2006) derived the shape-size relationship, while Yanovsky (2011) explored the effects of turbulence on spectral  $Z_{dr}$ . These studies were conducted at centimeter-wavelength frequencies.

In order to build quantitative retrieval algorithms based on spectral polarimetric observations, forward model simulators of the spectral polarimetric spectra themselves are needed. Simulations of Doppler spectra observed by ground-based vertically  
50 pointing radars have been pioneered by Zrnić (1975) and has been applied to different hydrometeors and to millimeter radars by different authors (e.g. Kollias et al., 2011b; Tridon and Battaglia, 2015; Courtier et al., 2024), also including turbulence effects and raindrop inertia (Zhu et al., 2023). The simulation of spectral polarimetric spectra (Myagkov et al., 2020; Unal and van den Brule, 2024) has been explored only marginally because slant observations are not so common.

Rain electromagnetic scattering properties have been historically computed by assuming spheroidal or Chebyshev shapes  
55 (both rotationally symmetric) via the T-matrix method (Mishchenko et al., 2000). Such models have been found satisfactory to explain radar and radiometric measurements in the S, C, X, Ku and Ka band (Battaglia et al., 2010; Kumjian et al., 2019; Teng

et al., 2018) but they have also been used to simulate higher radar frequencies (Aydin and Lure, 1991; Kneifel et al., 2020; Unal and van den Brule, 2024). However, raindrops generally change due to oscillations, which cause departure from rotationally symmetric shape. The T-matrix method can, in principle, simulate scattering from non-rotationally symmetric particles (given numerical convergence; Wriedt 2002), but such implementations are computationally demanding and not widely available. As a result, most T-matrix applications rely on the assumption of rotationally symmetric particles. Different studies have highlighted the strong impact of the shape assumptions in modifying the polarimetric variables (e.g. Ekelund et al., 2020 compared sphere, spheroids and equilibrium/Chebyshev drops) particularly when considering particles in the resonance regions (Thurai et al., 2007) (that occur in the 5.5–7-mm-diameter region at C band and at smaller sizes and in multiple ranges when increasing frequency). Such studies however are based on study of the DSD-integrated polarimetric variables and therefore do not fully capture the impact of the shape on each single particle. Combining Doppler and polarimetric measurements spectral polarimetry has the potential to test hydrometeor shape models and their associated scattering properties in great detail.

Therefore, the first goal of this study is to explore how different assumptions that are related to atmospheric conditions (turbulence) and white ~~and stochastic~~ noise of a real radar spectrum, impact the simulated spectral polarimetric variables. The second objective is to present a novel comparison between simulated and observed data.

The paper is structured as following. First we detail the methodology for simulating the cloud radar spectra and polarimetric variables (Sect. 2); then we present the results of our simulations, describe the observational dataset, compare simulations and observations, and discuss the implications of our findings.

## 2 Methodology for simulations

### 2.1 Rain scattering properties simulated by T-matrix

The simulations are generated by using a Python package for computing the electromagnetic scattering properties of nonspherical particles using the T-matrix method (Leinonen, 2014).

In this study, the rain scattering properties are exclusively targeted. The backscattering amplitude matrix,  $S$ , and the phase matrix,  $Z$ , (Chapt. 16 in Mishchenko et al., 2000) are calculated for drops of different diameters  $D$ , with axis ratios parameterized according to ~~Keenan et al. (2001); Andsager et al. (1999); Beard and Chuang (1987); Bringi and Chandrasekar (2001)~~ [Keenan et al. \(2001\); Andsager et al. \(1999\); Beard and Chuang \(1987\)](#). In the following, Eq. (1) is employed to describe the raindrop axis ratio:

$$\frac{a}{b}(D) = \begin{cases} 1/(0.9939 + 0.00736 \cdot D - 0.018485 \cdot D^2 + 0.001456 \cdot D^3) & D < 0.89 \text{ mm} \\ 1/(1.0048 + 5.7 \cdot 10^{-4} D - 2.628 \cdot 10^{-2} D^2 + 3.682 \cdot 10^{-3} D^3 - 1.677 \cdot 10^{-4} D^4) & D \geq 0.89 \text{ mm} \end{cases} \quad (1)$$

where  $a/b$  denotes the ratio of the major to minor axis of the oblate spheroid. [The use of two different formulations reflects the physical differences in raindrop deformation regimes.](#) For small raindrops, the axis ratio follows the parameterization by

Keenan et al. (2001), while for larger drops, the ~~formulation of Beard and Chuang (1987) is applied~~ fit of Andsager et al. (1999) to the Beard and Chuang (1987) model is used.

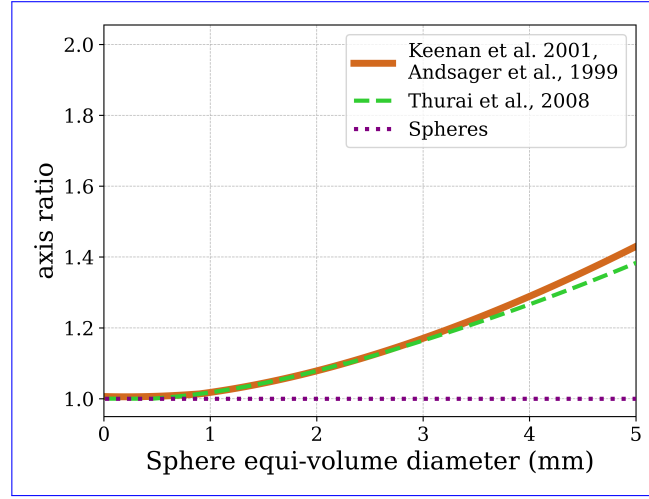


**Figure 1.** Axis ratio (major to minor axis) parametrization as a function of equi-volume diameters. The brown line is used in this study and is calculated according to ~~Keenan et al. (2001); Andsager et al. (1999); Beard and Chuang (1987); Bringi and Chandrasekar (2001)~~ Keenan et al. (2001); Andsager et al. (1999). The green dashed line is the parametrization of Thurai et al. (2008) and the purple dotted line is the axis ratio of spheres.

The brown line in Figure 1 represents the axis ratio parametrization used in this study, and is plotted against the equivalent relationship of Thurai et al. (2008) (green dashed line) and the axis ratio of spheres (purple dotted line). The first two lines present great agreement for particles with equi-volume diameter up to 3 mm. Very small droplets are conceived as perfect spheres (axis ratio  $\approx 1$ ). As their size increases, drops are modelled as spheroidal particles and an oblate shape is assumed (axis ratio  $> 1$ ). The scattering geometry of the simulation corresponds to a radar pointing at a  $45^\circ$  elevation angle. Raindrops are assumed to be partially aligned with their maximum dimension preferentially on the horizontal plane: scattering properties are averaged over Gaussian distributions of canting angles with different standard deviations. The raindrops are assumed to be at  $10^\circ\text{C}$  and the ~~refractive index~~ complex relative permittivity of water at this temperature is  $3.2 - 1.8j$  at 94 GHz (Lhermitte, 1990).

### 2.1.1 Computation of single-particle Polarimetric Variables

The phase matrix  $Z$  describes how an electromagnetic wave is scattered by a particle and how the scattering affects its polarization state (Mishchenko et al., 2000). It is a  $4 \times 4$  matrix that transforms the Stokes vector of an incident electromagnetic wave into the Stokes vector of the scattered wave. From the elements  $Z_{ij}(\mathbf{D})$  of this matrix the following backscattering quantities can be computed:



- Backscattering cross sections for V-polarized and H-polarized radiation:

$$\begin{aligned}\sigma_{VV}(D) &= 2\pi(Z_{11} + Z_{12} + Z_{21} + Z_{22}) & [\text{mm}^2] \\ \sigma_{HH}(D) &= 2\pi(Z_{11} - Z_{12} - Z_{21} + Z_{22}) & [\text{mm}^2]\end{aligned}\tag{2}$$

- Differential reflectivity

$$105 \quad Z_{DR}(D) = 10 \log_{10} \frac{\sigma_{HH}(D)}{\sigma_{VV}(D)} \quad [\text{dB}]\tag{3}$$

- Copolar correlation coefficient

$$\rho_{HV}(D) = \frac{\sqrt{(Z_{33} + Z_{44})^2 + (Z_{43} - Z_{34})^2}}{\sqrt{(Z_{11} - Z_{12} - Z_{21} + Z_{22})(Z_{11} + Z_{12} + Z_{21} + Z_{22})}}\tag{4}$$

- Differential Phase

$$\delta_{HV}(D) = \arctan \left( \frac{Z_{43} - Z_{34}}{Z_{33} + Z_{44}} \right) \quad [\text{degrees}]\tag{5}$$

110 The normalised backscattering cross section of an oblate spheroidal raindrop is shown in Fig. 2 with brown color. The axis ratio for this computation is the same as the brown line of Fig. 1. The dashed green line represent the same quantity, but computed by using the Thurai et al. (2008) axis ratio parametrization (green line in Fig. 1). The same applies for the purple dotted line which is produced by using the spheres' axis ratio. The two different spheroids parametrizations result in nearly identical curves, indicating that the choice of axis ratio for oblate shapes does not significantly affect the backscattering  
115 cross section behavior. In contrast, the spherical parametrization shifts the Mie notches slightly to the left, due to the different geometry of the scatterers. The positions of the first, second, and third Mie notches, are indicated by the blue dashed lines at  $D = 1.68 \text{ mm}$ ,  $D = 2.88 \text{ mm}$ , and  $D = 4.13 \text{ mm}$ , respectively.

Some T-matrix results for the polarimetric variables are displayed in Fig. 3 and 4: different drop orientation conditions and raindrops axis ratios are considered. The black dashed and the blue lines are calculated by assuming perfectly oriented  
120 raindrops with axis ratio parametrization as proposed by Thurai et al. (2008) and according to Eq. 1, respectively. ~~Those~~ In Fig. 3 those two lines are almost identical up to approximately 3 mm diameters but they diverge afterwards. Notably, for larger raindrops, the black dashed line aligns closely with the light blue line, which represents a wobbling raindrop with a  $5^\circ$  canting angle on average. This suggests that the same amplitude of the maxima and minima in the spectral polarimetric variables can be achieved by different combinations of axis ratio parameterizations and varying degrees of wobbling. Therefore in the following  
125 the parametrization of Eq. 1 is used in combination with different degrees of wobbling.

The differential phase ( $\delta_{HV}$ ) refers to the phase shift introduced at backscattering between the horizontally and vertically polarized components of the received radar signal. ~~providing information about the~~ This parameter depends on the size of the hydrometeors and provides information about their shape and orientation ~~of hydrometeors~~. In Fig. 3 (right),  $\delta_{HV}$  remains near zero for small drop diameters, consistent with Rayleigh scattering. As the diameter increases,  $\delta_{HV}$  departs from zero

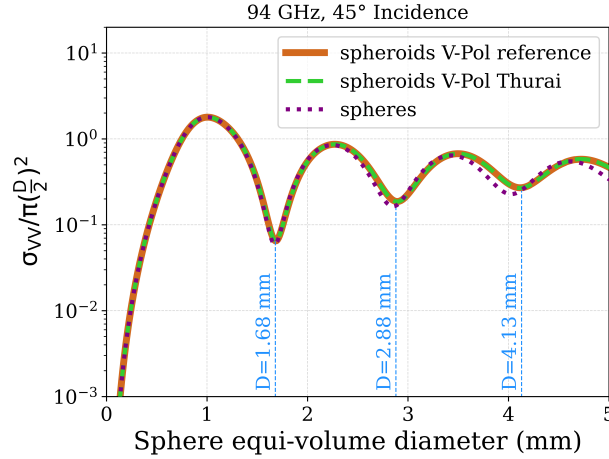


**Figure 2.** Normalised backscattering cross section of oblate spheroidal model raindrops when pointing at  $45^\circ$  elevation as function of the sphere equi-volume diameter  $D$ . The light blue dashed lines indicate the first ( $D = 1.68$  mm), second ( $D = 2.88$  mm), and third ( $D = 4.13$  mm) Mie notches.

130 and exhibits oscillatory behavior, attributed to resonance effects and the transition from spherical to oblate shapes. These fluctuations become more pronounced at larger diameters. Variability in drop orientation within the radar sampling volume, described by canting angle distributions, further contributes to the observed variations in  $\delta_{HV}$ . The broader the width of the canting angle distribution is, the lower the magnitude of the polarimetric variables. When particles are randomly oriented (red line in Fig. 3), their orientations are distributed uniformly in all directions. In this case, the ensemble-averaged response  
135 over all possible orientations lead to cancellation effects in the differential phase ( $\delta_{HV}=0$ , Fig. 3-right) and in the differential reflectivity ( $Z_{DR}=0$  dB, Fig. 3-left). The cancellation occurs because, for a medium which is a mixture of randomly oriented particles, the off-diagonal elements  $Z_{12}$ ,  $Z_{21}$ ,  $Z_{34}$ ,  $Z_{43}$  of the phase matrix become zero (as shown in Mishchenko et al. (2000), Chapter 3, Table II), thus leading to zero  $Z_{DR}$  and  $\delta_{HV}$  (see Eq. (3)-(5)). The blue dashed lines of Fig. 3 and 4 indicate the positions of the Mie notches, as depicted in Fig. 2. The first two minima of  $\delta_{HV}$  coincide with the Mie notches, while the  
140  $Z_{DR}$  is approximately zero at these points. Moreover, the diameters of the minima ( $D_1, D_3, D_5$ ), and maxima ( $D_2, D_4, D_6$ ), are demonstrated for  $Z_{DR}$ .

The copolar correlation coefficient ( $\rho_{HV}$ ) quantifies the correlation between the horizontally and vertically polarized components of the radar signal. In Fig. 4, perfectly oriented drops (blue and black dashed lines) have  $\rho_{HV}=1$ . On the other hand, ~~rain drops with~~ raindrops with variations in orientation or tilt of the drop axis relatively to the direction of motion (canting)  
145 have  $\rho_{HV}$  slightly lower than 1, showing a minimum loss of correlation between the two different polarization states. A broader distribution of canting angles would lead to further decorrelation. Even when considering randomly oriented raindrops  $\rho_{HV}$  never falls short of 0.986. Realistic values of canting generally do not exceed  $10^\circ$  (Mishchenko et al., 2000). However, neither

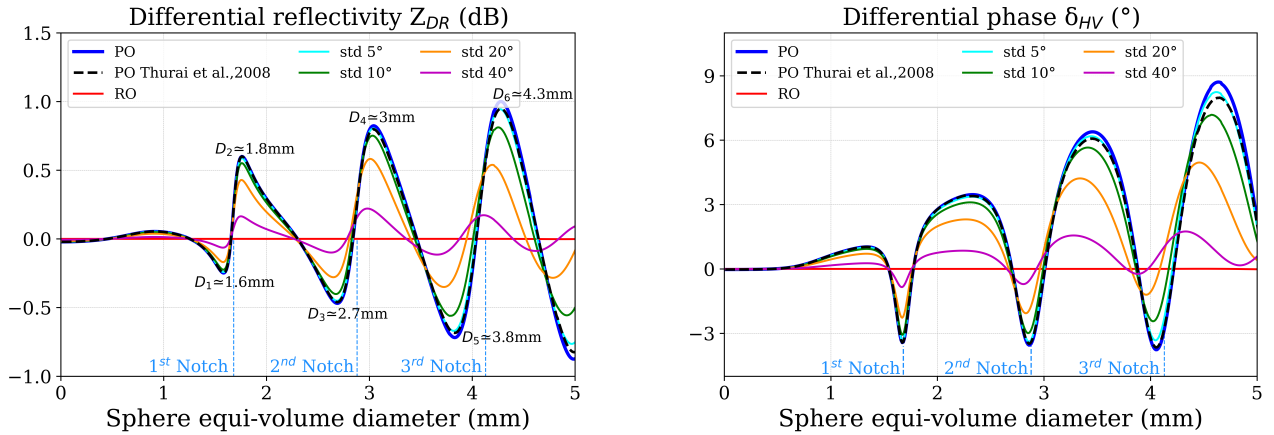


**Figure 3.** Simulations of differential reflectivity  $Z_{DR}$  (left) and differential phase  $\delta_{HV}$  (right) as a function of sphere **equi-volume** equi-volume diameters, for a 94 GHz radar pointing at  $45^\circ$ . PO (Perfect Orientation) and RO (Random Orientation) are represented by the dark blue and red lines, respectively, derived with axis ratio parametrization according to Eq. (1). The black dashed line corresponds also to perfectly oriented raindrops with axis ratio parameterization as proposed by Thurai et al. (2008). The remaining lines represent different degrees of raindrop wobbling, with a Gaussian distribution around the horizontal with standard deviations of  $5^\circ$  (light blue),  $10^\circ$  (green),  $20^\circ$  (orange), and  $40^\circ$  (pink).

antenna pattern effects, nor antenna coupling for the quasi-bistatic radar configuration, nor multiple scattering, nor noise were included in the calculations of  $\rho_{HV}$  at this stage. One or a combination of these effects may drive  $\rho_{HV}$  below 0.986.

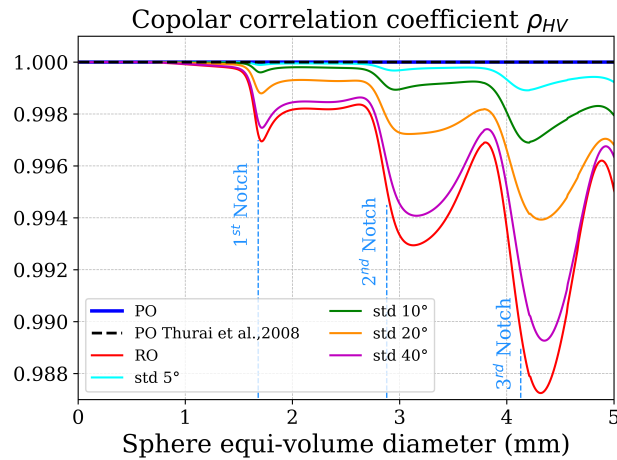


**Figure 4.** Same as in Fig. 3 for the copolar correlation coefficient  $\rho_{HV}$  as a function of sphere **equi-volume** equi-volume diameters, for a 94 GHz radar pointing at an elevation of  $45^\circ$ .

## 150 2.1.2 Drop Size Distribution and Raindrop Velocities

The gamma distribution is a mathematical shape typically used to represent the variability of a natural rainfall Drop Size Distribution (DSD) (Ulbrich, 1983):

$$N(D) = N_0 D^\mu \exp(-\Lambda D) \quad [mm^{-1}m^{-3}] \quad (6)$$

155  $D$  [mm] is the sphere equi-volume diameter,  $\mu$  is the dimensionless shape parameter,  $N_0$  [ $mm^{-1-\mu}m^{-3}$ ] is the number concentration parameter and  $\Lambda$  [ $mm^{-1}$ ] is the slope parameter. The three parameters ( $N_0$ ,  $\mu$ , and  $\Lambda$ ) of the gamma distribution enable a wide range of rainfall situations to be described.  $\Lambda$  can be derived from  $\Lambda = \frac{4+\mu}{D_m}$ , where  $D_m$  [mm] is the mass-weighted mean diameter (Ulbrich and Atlas, 2007; Testud et al., 2001).

160 Important for Doppler applications, the larger the drops, the faster the terminal fall speed,  $v_T$ . The relationship between the drop diameters and the corresponding velocities is parameterized in SI units following Frisch et al. (1995) and Atlas et al. (1973):

$$v_T(D) = \begin{cases} v_{cloud} = 1.2 \cdot 10^8 \cdot \left(\frac{D}{2}\right)^2 & D < 0.11 \cdot 10^{-3} \text{ m} \\ v_{drizzle} = 8333 \cdot \frac{D}{2} - 0.0833 & 0.11 \cdot 10^{-3} \leq D \leq 0.86 \cdot 10^{-3} \text{ m} \\ v_{rain} = 9.65 - 10.3 \cdot e^{-0.6 \cdot 10^3 \cdot D} & D > 0.86 \cdot 10^{-3} \text{ m} \end{cases} \quad (7)$$

A factor  $\left(\frac{\rho_0}{\rho}\right)^{0.4}$  with  $\rho_0$  being the density at sea level applies for different air densities.

165 In Fig. 5, raindrop terminal velocities are plotted against the diameters according to Eq. (7) and the parametrization from Thurai and Bringi (2005) (brown and dashed black line, respectively). The relative difference between the two velocity parametrizations never exceeds 2%. Therefore, when mapping terminal velocities into diameters, this translates into similar relative uncertainties in the determination of diameters for any given velocity. For instance the position of the first (second) Mie notch is expected to occur at terminal velocities of  $5.89 \pm 0.11 \text{ m/s}$  ( $7.82 \pm 0.15 \text{ m/s}$ ).

## 2.2 Simulation of spectral polarimetric variables

170 Two methodologies for simulating spectral polarimetric variables as observed from a W-band cloud radar will be presented in this paper. The first was developed based on (Yu et al., 2012; Zrnić, 1975), while the second on (Thurai et al., 2008) and (Chandrasekar, 1986). Notably, both methods show very good agreement and will be described in detail in Secs. 2.2.1, 2.2.2. The use of both approaches ensures that the introduced stochastic perturbations respect the physical relationships between scattering elements. Their agreement increases confidence in the simulated turbulence structure and supports that observed discrepancies are not artifacts of the simulation method. Some preliminary processing is needed for both methodologies as discussed below.

Firstly an ideal co-polar spectrum  $S_{VV}$  for the V-channel is independently generated for each diameter (Unal, 2015) :

$$S_{VV}(v_{LoS}) = \frac{\lambda^4}{\pi^5 |K|^2} N(D) \sigma_{VV}(D) \frac{1}{\sin \theta_{el}} \frac{dD}{dv_T(D)} \quad (8)$$

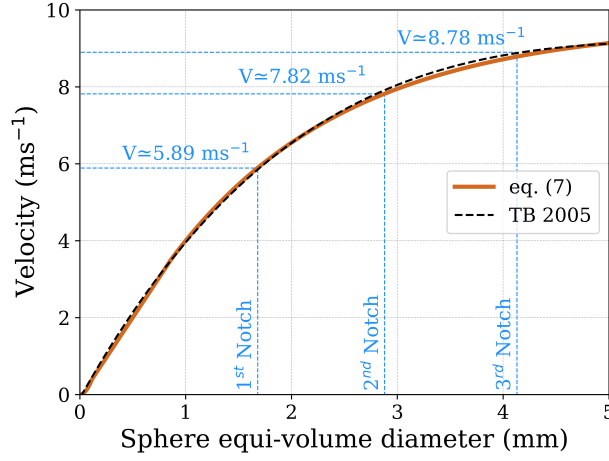


**Figure 5.** Terminal fall speed  $v_T$  as a function of the sphere equi-volume diameter  $D$ , for equation (7) with brown thick line, and for Thurai and Bringi (2005) with dashed black line.

where  $\lambda$  is the radar wavelength,  $|K^2|$  is derived from the dielectric factor of water,  $N(D)$  is the DSD (see Sec. 2.1.2),  $\sigma_{VV}$  is the backscattering cross section for V channel (Sect. 2.1.1) and  $v_{LoS}(D) = \sin \theta_{el} v_T(D) + w_{LoS}$  denotes the Line of Sight (LoS) Doppler velocities of the drops at the given elevation angle  $\theta_{el}$ .  $v_{LoS}$  is the sum of the component of the raindrop terminal velocity and of the wind speed along the LoS. Eq. (8) is formulated for elevation angles  $\theta_{el}$  significantly greater than zero, without accounting for the contribution of turbulence. The spectrum is mapped into the velocity domain via Eq. (7) and sampled in correspondence to the velocity points  $v_j$  with  $j = 1, 2, \dots, N_{FFT}$  where  $N_{FFT}$  is the number of FFT points as dictated by the Doppler velocity resolution and Nyquist interval envisaged for any given radar system. The samples are indicated with  $S_{VV}(v_j)$ . Similarly, H-channel spectrum can also be produced at each velocity bin by replacing  $\sigma_{VV}(D)$  with  $\sigma_{HH}(D)$  in Eq. (8).

The cross spectrum, denoted as  $S_{HV}(D)$ , is derived as follows:

$$S_{HV}(v_{LoS}) = \frac{\lambda^4}{\pi^5 |K|^2} N(D) \sqrt{\sigma_{VV}(D) \sigma_{HH}(D)} \frac{1}{\sin \theta_{el}} \frac{dD}{dv_T(D)} \rho_{HV}(D) e^{i\delta_{HV}(D)} \quad (9)$$

where  $\iota = \sqrt{-1}$ ,  $\rho_{HV}(D)$  is the correlation coefficient between the V and H channels, and  $\delta_{HV}(D)$  is the phase difference between the V and H channel signals, as described in Eqs. (4-5). The spectrum is sampled similarly to the V channel spectrum at velocity points  $v_j$  with  $j = 1, 2, \dots, N_{FFT}$ , and the samples are denoted as  $S_{HV}(v_j)$ . Note that each Doppler velocity spectrum can be converted into the frequency domain by using the relationship  $f_D = \frac{2v_{LoS}}{\lambda}$  between frequency Doppler shift,  $f_D$ , and  $v_{LoS}$ .

Generally spectra are derived at any given range via FFT of the time series of radar sampled voltage signals, the so called  $I$  (in-phase) and  $Q$  (quadrature) signals collected at the same range distance (Doviak and Zrnić, 1993). In the following complex

voltages will be identified with calligraphic style letters (e.g.  $\mathcal{V}, \mathcal{N}$ ). Also, such voltages will be always expressed in the velocity domain as indicated by their functional argument. They correspond to the FFT of the voltages expressed in the time domain.

### 2.2.1 Methodology I: direct computation of $I$ and $Q$ s in the frequency domain

This method allows Doppler spectra to be simulated by working only in the velocity (frequency) domain. Following Yu et al. (2012) the time series of complex voltage signal in the V channel in the velocity domain can be written as:

$$\mathcal{V}_V^{[1]}(v_j, k) = \sqrt{-S_{VV}(v_j) \ln u_{jk}^{[1]}} e^{i\theta_{jk}^{[1]}} \quad \begin{matrix} j=1, 2, \dots, N_{\text{FFT}} \\ k=1, 2, \dots, K \end{matrix} \quad (10)$$

where  $u^{[1]}$  and  $\theta^{[1]}$  are independent, identically distributed random variables with uniform distribution between 0 and 1 and between  $-\pi$  and  $\pi$ , respectively. This process can be repeated  $k = 1, 2, \dots, K$  times, in order to generate  $K$  independent stochastic realizations of the same spectrum. Similarly, for the H channel in the velocity domain:

$$\begin{aligned} \mathcal{V}_H(v_j, k) = & \sqrt{sZ_{DR}(v_j)[s\rho_{HV}(v_j)]} \mathcal{V}_V^{[1]}(v_j, k) \\ & + \sqrt{1 - s\rho_{HV}^2(v_j)} \mathcal{V}_V^{[2]}(v_j, k) e^{i s\delta_{HV}(v_j)} \end{aligned} \quad \begin{matrix} j=1, 2, \dots, N_{\text{FFT}} \\ k=1, 2, \dots, K \end{matrix} \quad (11)$$

where the spectral variables  $s\rho_{HV}$ ,  $s\delta_{HV}$  and  $sZ_{DR}$  are generated as described in Sect. 2.1 for each velocity bin  $j$ , but also hold the prefix  $s$  in the notation to differentiate them from the commonly used integral polarimetric variables.  $\mathcal{V}_V^{[2]}(v_j, k)$  is generated according to (10) with the same model spectrum  $S_{VV}(v)$ , but with a second independent sequence of random numbers ( $u^{[2]}$  and  $\theta^{[2]}$ ). This process is repeated for each velocity bin for a total of  $N_{\text{FFT}}$  spectral points within the Nyquist interval. The inverse Fourier transform of  $\mathcal{V}_V(v_j)$  and  $\mathcal{V}_H(v_j)$  with  $j = 1, 2, \dots, N_{\text{FFT}}$  represent simulated time series of complex signals for the V and H channels. For the implementation of white noise, an approach similar to Eq. (10) is used:

$$\begin{aligned} \mathcal{N}_V(v_j, k) &= \sqrt{-N_V \ln u_{jk}^{[3]}} e^{i\theta_{jk}^{[3]}} \\ \mathcal{N}_H(v_j, k) &= \sqrt{-N_H \ln u_{jk}^{[4]}} e^{i\theta_{jk}^{[4]}} \end{aligned} \quad \begin{matrix} j=1, 2, \dots, N_{\text{FFT}} \\ k=1, 2, \dots, K \end{matrix} \quad (12)$$

where  $N_V$  and  $N_H$  are the noise power levels for the V and H channel corresponding to the prescribed values of signal-to-noise ratios ( $SNR$ ), and  $u^{[3]}$ ,  $\theta^{[3]}$ ,  $u^{[4]}$ ,  $\theta^{[4]}$  are again generated independently.

The complex numbers that represent the simulation of the noisy  $I$  and  $Q$ s in the frequency domain for the V and H channels are calculated from:

$$\begin{aligned} S_V(v_j, k) &= \mathcal{V}_V(v_j, k) + \mathcal{N}_V(v_j, k) \\ S_H(v_j, k) &= \mathcal{V}_H(v_j, k) + \mathcal{N}_H(v_j, k) \end{aligned} \quad \begin{matrix} j=1, 2, \dots, N_{\text{FFT}} \\ k=1, 2, \dots, K \end{matrix} \quad (13)$$

### 2.2.2 Methodology II: correlation matrix

Alternatively the  $I$  and  $Q$  generation can be performed using the methodology proposed by Unal and Moiseev (2004) based on the correlation matrix. First the correlation matrix  $R$  is built with the Doppler power spectra in the diagonal terms and the cross-polar spectrum in the antidiagonal elements as:

$$R(v_j) = \begin{pmatrix} S_{VV}(v_j) + N_V & S_{HV}(v_j) \\ S_{HV}^*(v_j) & S_{HH}(v_j) + N_H \end{pmatrix} \quad j = 1, 2, \dots, N_{\text{FFT}} \quad (14)$$

with all terms given by Eqs. (8-9). Noise has also been included but with no copolar correlation. Because  $R$  is Hermitian and positive definite, it may be written as  $R = T^\dagger T$  via Cholesky decomposition, where  $^\dagger$  denotes Hermitian transpose. Given  
225  $2N_{FFT}$  zero-mean independent standard circular Gaussian random variables,  $y_1, y_2, \dots, y_{2N_{FFT}}$  [i.e.  $y_j = 1/\sqrt{2}(\xi_j + \imath \eta_j)$  where  $\xi_j$  and  $\eta_j$  are normally distributed with mean equal 0 and standard deviation equal 1], the complex numbers

$$\begin{bmatrix} \mathcal{S}_V(v_1) \\ \mathcal{S}_H(v_1) \\ \mathcal{S}_V(v_2) \\ \mathcal{S}_H(v_2) \\ \vdots \\ \mathcal{S}_V(v_{FFT}) \\ \mathcal{S}_H(v_{FFT}) \end{bmatrix} = T^\dagger \begin{bmatrix} y_1 \\ y_2 \\ y_3 \\ y_4 \\ \vdots \\ y_{2N_{FFT}-1} \\ y_{2N_{FFT}} \end{bmatrix} \quad (15)$$

have components distributed as normally distributed variables with zero mean and with correlation provided by  $R$ . The procedure can be repeated  $K$ -times to simulate  $K$  different spectra.

### 230 2.2.3 Computation of polarimetric variables from $I$ and $Q$ s

Once the  $I$  and  $Q$ s are obtained with either of the two methodologies, then noisy Doppler spectra can be computed as a spectral average of  $K$  spectra as:

$$S_{VV}(v_j) = \langle |\mathcal{S}_V(v_j)|^2 \rangle = \frac{1}{K} \sum_{k=1}^K |\mathcal{S}_V(v_j, k)|^2 \quad (16)$$

$$S_{HH}(v_j) = \langle |\mathcal{S}_H(v_j)|^2 \rangle = \frac{1}{K} \sum_{k=1}^K |\mathcal{S}_H(v_j, k)|^2 \quad (17)$$

235 The spectral polarimetric variables  $s\rho_{HV}(v)$  and  $s\delta_{HV}(v)$  are calculated according to Mishchenko et al. (2000):

$$s\rho_{HV}(v_j) e^{\imath s\delta_{HV}(v_j)} = \frac{\langle \mathcal{S}_H(v_j) \mathcal{S}_V^*(v_j) \rangle}{\sqrt{\langle |\mathcal{S}_H(v_j)|^2 \rangle \langle |\mathcal{S}_V(v_j)|^2 \rangle}} \quad (18)$$

where  $\langle \mathcal{S}_H(v_j) \mathcal{S}_V^*(v_j) \rangle$  is the average  $\frac{1}{K} \sum_{k=1}^K \mathcal{S}_H(v_j, k) \mathcal{S}_V^*(v_j, k)$ .

### 2.2.4 Inclusion of turbulence in the simulations

Understanding the effects of turbulence on the Doppler spectrum is crucial for improving the accuracy of radar observations  
240 and their interpretation. Atmospheric turbulence causes random fluctuations in the velocity of hydrometeors, thus broadening the Doppler spectrum. All droplets are here assumed to have no inertial effects and therefore act like perfect tracers. Thus, to introduce the turbulent motions of drops in the simulations, the Doppler spectra must be convolved with a turbulence term

$S_{air}$ :

$$S_{VV}^{turb}(v_{LoS}) = (S_{VV} * S_{air})(v_{LoS}) = \int_{-\infty}^{\infty} S_{VV}(v_{LoS} - \xi) S_{air}(\xi) d\xi \quad (19)$$

245 where  $\xi$  is the convolution variable and  $S_{air}$  accounts for the turbulent motions within the atmosphere:

$$S_{air}(v) = \frac{1}{\sqrt{2\pi}\sigma_t} e^{-\frac{v^2}{2\sigma_t^2}} \quad (20)$$

with  $\sigma_t$  expressing the turbulence broadening of the Doppler spectrum. Equations similar to Eq. (19) can be used to compute the turbulence-broadened spectra  $S_{HH}^{turb}(v)$  for H-polarized radiation, as well as for  $S_{HV}^{turb}(v)$ . Then the broadened  $sZ_{DR}^{turb}(v)$  can be computed as the ratio of  $S_{HH}^{turb}(v)$  to  $S_{VV}^{turb}(v)$  whereas the turbulent-broadened parameters  $s\rho_{HV}^{turb}$  and  $s\delta_{HV}^{turb}$  are then  
250 calculated respectively as the amplitude and the phase of the variable:

$$s\rho_{HV}^{turb}(v)e^{is\delta_{HV}^{turb}(v)} = \frac{S_{HV}^{turb}(v)}{\sqrt{S_{HH}^{turb}(v)S_{VV}^{turb}(v)}} \quad (21)$$

For the generation of the  $I$  and  $Q$ s:

- for methodology 1 (Sect. 2.2.1) the simulated spectral polarimetric variables  $sZ_{DR}^{turb}(v)$ ,  $s\delta_{HV}^{turb}(v)$ ,  $s\rho_{HV}^{turb}(v)$  will replace the ideal quantities in Eq. (11);
- 255 – for methodology 2 (Sect. 2.2.2)  $S_{VV}^{turb}$ ,  $S_{HH}^{turb}$ , and  $S_{HV}^{turb}$  are directly used in the definition of the correlation matrix in Eq. (14).

### 2.2.5 Rationale for simulation based on I/Q

The reason we chose to generate noisy spectra using I/Q components, instead of working with average spectra with added noise power, is to explicitly investigate whether the use of random individual noisy spectra can help explain or reproduce the variability and degradation often observed in measured spectral polarimetric variables, particularly in variables that rely on cross-channel correlations like  $S_{\overline{vv}}S_{HV}$ , at low SNR and low correlations where approximated formulas as ~~proposed~~ demonstrated in Myagkov and Ori (2022) tend to fail.

260

By simulating the noisy spectra from I/Q components, we aimed to test whether noise characteristics contribute to the spectral variability seen in observations. In this sense, our work seeks to fill a gap in the literature and offer an alternative angle  
265 to understanding the role of noise in radar polarimetry.

## 3 Comparisons with measurements

To assess the accuracy of the cloud radar simulation methods, we compare the measurements and the simulated data. This comparison aims to validate the performance of the simulations and identify any discrepancies that may arise from model



assumptions or parameter settings. The cloud radar measurements were obtained using a RPG Frequency Modulated Continuous Wave (FMCW) Dual Polarization W-band Cloud Doppler Radar, operating at 94 GHz in a simultaneous transmission - simultaneous reception (STSR) mode. The radar system was configured to investigate polarimetric and spectral polarimetric measurements of clouds and precipitation in the troposphere during four months (January-April 2021). The models described in 2.2.1, 2.2.2 were initialized based on the characteristics (SNR, PRF, FFT bins) of the real measurements to generate simulated radar data for the comparison with the real data.

Two case studies from 3 February 2021 are presented, both characterized by moderate rainfall, with rain rates approximately between 6 and 7 mm/h. The first one focuses on a spectrum acquired at an altitude of 105 meters above ground level, while the second one targets a spectrum at 484 meters. The cases differ primarily in the level of atmospheric turbulence observed at specific heights. ~~Higher altitudes are usually~~ Excluding cases of strong wind shear (e.g., jet streams) and deep convective systems (e.g., thunderstorms), higher altitudes are generally characterized by significantly less turbulence ~~relatively to than~~ lower levels, ~~because turbulence is often as~~ turbulence is mostly generated by surface heating and friction. The measured spectrogram on the vertical channel  $S_V$ , and the polarimetric variables  $sZ_{DR}$ ,  $s\delta_{HV}$  and  $s\rho_{HV}$ , are presented in Fig. 6. The x-axis represents the Doppler velocity,  $v_{LoS}$ , corresponding to the unfolded measured Doppler velocity. The spectral signatures associated with small raindrops appear on the left side of the spectra. As raindrop sizes increase and become comparable to the radar wavelength, non-Rayleigh scattering occurs, leading to resonance features observed on the right side of the spectra.

To facilitate the comparison between simulations and observational data, the terminal velocity,  $v_T$ , was selected for the velocity axis in Sect. 3.1 and 3.2. Accordingly, the Doppler velocities shown in Fig. 6 were first adjusted along the velocity axis to remove the contribution of the radial wind,  $w_{LoS}$ . This correction was achieved by identifying the first Mie scattering minimum (Kollias et al., 2002). At an elevation angle of  $\theta_{el}=45^\circ$ , the first Mie minimum corresponds to a velocity of  $5.89 \sin \theta_{el} = 4.16 \text{ ms}^{-1}$ . The resulting corrected Doppler velocities,  $v_{LoS} - w_{LoS}$ , were then divided by  $\sin \theta_{el}$ , yielding an estimate of the terminal velocities for the observations.

A comparison between measured and simulated  $s\rho_{HV}$  is challenging. The measurement of  $s\rho_{HV}$  is subjected to biases (particularly at low signal-to-noise levels, (Touzi et al., 1999)) and is affected by radar-specific characteristics (e.g. antenna-related) which are difficult to be quantified and accounted for (Myagkov et al., 2024). Therefore  $s\rho_{HV}$  is not further analyzed in this paper.

### 3.1 Case Study 1: Moderate turbulence conditions

The Doppler spectrum measured at a height of 105 m is presented in Figure 7 with a black line. The presence of turbulence is depicted on the broadening effect of the spectrum and the notches are smoothed out. To accurately match the measured radar spectrum, a variety of gamma Drop Size Distributions (DSDs) were produced by adjusting the parameters described in 2.1.2, aiming to find the DSD that best fit the observed spectrum (blue line). Different combinations of  $\mu$ ,  $N_0$ ,  $D_m$  (from eq. 6) and  $\sigma_t$  (from eq. 20) are tested to better represent the real measurement. To identify the optimal fit, the Least Squares Method was employed. This method minimizes the sum of the squared differences between the measured and simulated spectra, ensuring that the best-fitting gamma DSD is selected. The spectra are compared in logarithmic scale rather than in linear units to better

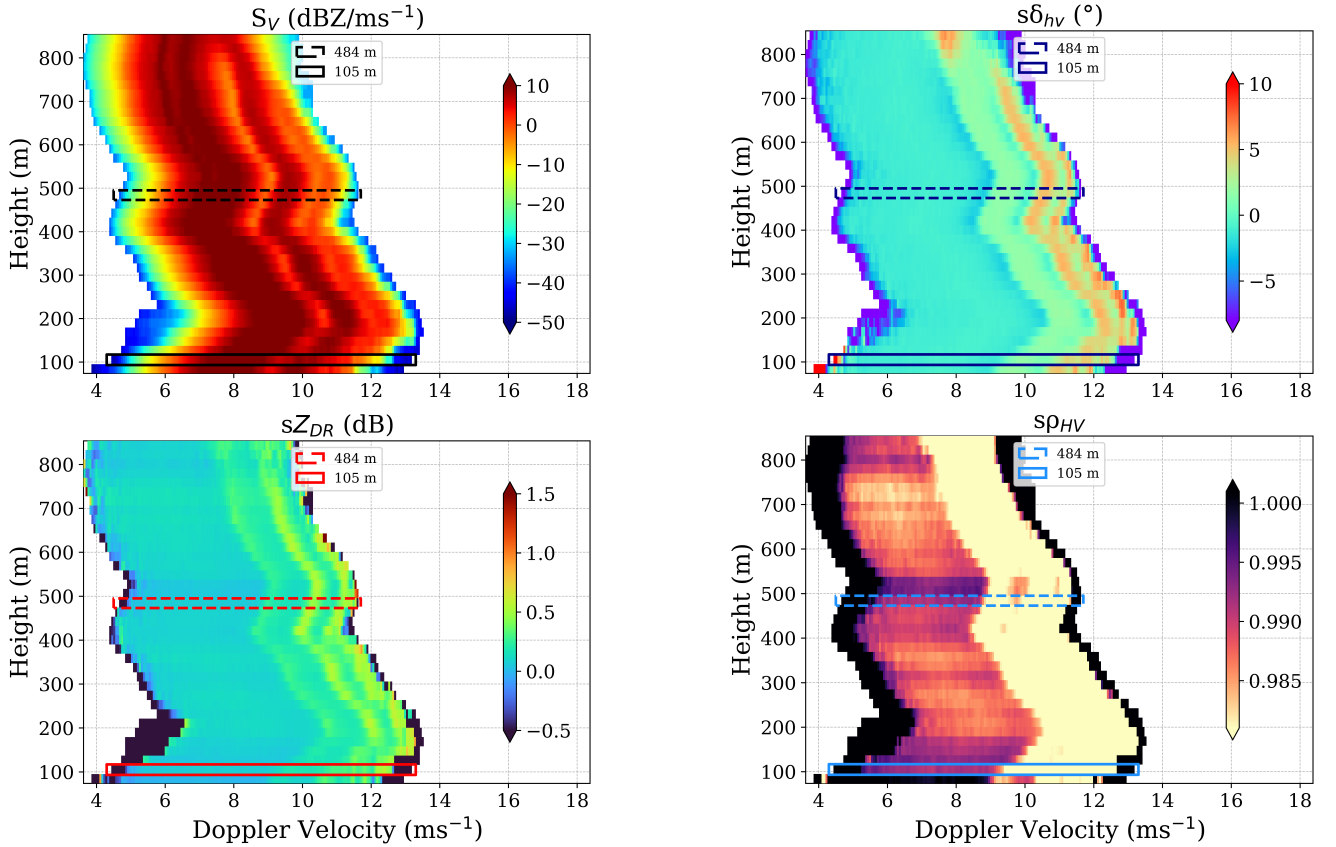


**Figure 6.** Event of 03 Feb 2021, 12:40 UTC with vertical profiles for reflectivity (top left), differential reflectivity (bottom left), differential phase shift (top right), correlation coefficient (bottom right) spectra. The two levels that are used for case studies are marked by the solid (105 m) and dashed (484 m) rectangles.

capture the wide dynamic range of radar reflectivity. This way, both high and low reflectivity values are appropriately weighted, avoiding dominance by large values that occur in linear comparisons. In order to avoid overfitting the tails of the spectrum (and  
 305 deteriorating the fits of the high SNR part of the spectrum, e.g. in correspondence to the Mie notch), only the part of the spectrum above the purple dashed line at  $-8 \text{ dBZ/ms}^{-1}$  is fitted. That emphasizes the resonance notches—whether sharp or smoothed—providing a more robust indication of the magnitude of  $\sigma_t$ . This threshold is an empirical rule of thumb derived from this study, which primarily focused on cases with rain rates between 5-9 mm/hr.

In Figure 8, the black lines represent the measured spectral polarimetric variables  $sZ_{DR}$  (left) and  $s\delta_{HV}$  (right), while the  
 310 blue and red lines are the results of the two simulation methods. The, by using the above mentioned optimum-fitted Doppler spectrum (see Fig. 7). Next to the radar elevation angle, the primary physical factors influencing the spectral polarimetric variables are the axis ratio–diameter relationship, and the canting angle distribution (Unal and van den Brule (2024)), and

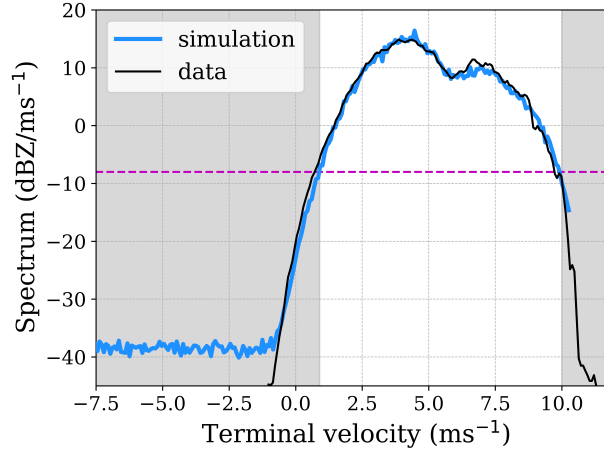


**Figure 7.** 03 February 2021, 12:40 UTC, 105m, Measured Doppler Spectrum (black line) and optimum-fitted Gamma DSD (blue line). The purple dashed line indicates the threshold for applying the Least Squares Method in order to find the optimum fit. The parameters that characterize the fitted spectrum are  $\mu = 0$ ,  $D_m = 1.8 \text{ mm}$ ,  $N_0 = 987 \text{ mm}^{-1-\mu} \text{ m}^{-3}$ , and  $\sigma_t = 0.5 \text{ ms}^{-1}$

variability in air motion, characterized by  $\sigma_t$ . The ~~particle size distribution has a comparatively minor impact on these variables. When  $\sigma_t = 0$ , the spectral polarimetric variables become independent of the PSD. values of  $sZ_{DR}$  and  $s\delta_{HV}$  do not depend~~  
 315 on the raindrop size distribution (Unal and van den Brule (2024)). However, what may vary in Figure 8 is the terminal velocity range—for example, under low turbulence conditions, the velocity range narrows when  $D_m$  is small, as in the case of light rain.

In order to provide a consistent reference for spherical raindrops the measured  $sZ_{DR}$  and  $s\delta_{HV}$  were adjusted along the y-axis to 0 dB and  $0^\circ$ , respectively. The adjustment was determined based on the measured values for the smallest particles,  
 320 which are expected to be nearly spherical. This correction accounts for propagation effects and instrument miscalibrations of the polarimetric variables. The spectral polarimetric variables are analyzed outside the gray-shaded regions, where the Doppler spectral power exceeds  $-8 \text{ dBZ/ms}^{-1}$ , to ensure a sufficiently high signal-to-noise ratio.

As expected, there is excellent agreement (within the stochastic noisiness) between the two methods used for generating the simulations (blue and red lines) for the two variables. The use of both methods described in Sect. 2.2 is to ensure that  
 325 the stochastic perturbations respect the physical relationships between the scattering elements. The fact that both methods demonstrate consistency when producing the polarimetric variables provides confidence in the turbulence generation on the simulations. On the other hand while the comparison between cloud radar simulations and measurements exhibits some agreement, there are notable discrepancies that indicate limitations in the current simulation models. The primary issue is not the position of the maxima and minima, but rather the amplitude of the signal (e.g. no negative  $sZ_{DR}$  is observed). Although the  
 330 position of the extrema may be slightly influenced by uncertainties in mapping diameters to velocity space (see Sect. 2.1.2), the key factor affecting their position is the scattering process itself. For drops with terminal velocities up to 7 m/s, the simulations

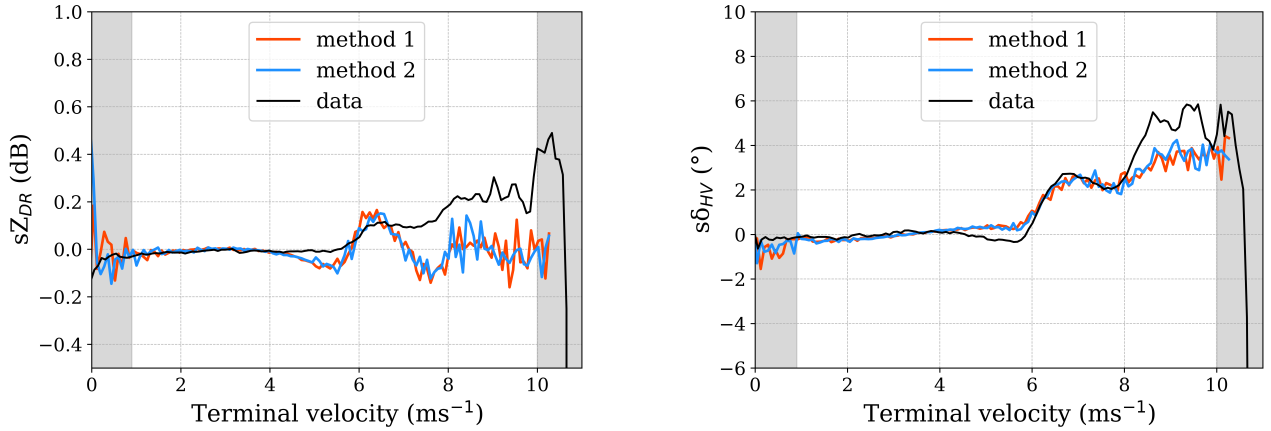


**Figure 8.** Spectral polarimetric variables of case study 1. Left panel: spectral differential reflectivity  $sZ_{DR}$ , Right panel: spectral differential phase  $s\delta_{HV}$ . The black lines represent the measured data, the blue and red lines represent the simulations from method 1 and method 2 respectively.

and the observations of  $sZ_{DR}$  and  $s\delta_{HV}$  show reasonable agreement. Although, around velocities of 5 m/s, smaller values of  $sZ_{DR}$  and bigger values of  $s\delta_{HV}$  are simulated relatively to the observations. However for drops with higher terminal velocities ( $v_T > 7 \text{ ms}^{-1}$ ), the agreement between observations and simulated data is poor, especially for the differential reflectivity.

335 Note these results are obtained with perfectly oriented raindrops. When increasing the canting the amplitude of both  $sZ_{DR}$  and  $s\delta_{HV}$  are reduced and a worse correlation is obtained.

### 3.2 Case Study 2: Light turbulence conditions

In this case, the notches of the Doppler spectrum are more pronounced (Fig. 9). The best-fitting gamma DSD is represented by the blue line.

340 In the subsequent analysis, only one simulation method is presented, as the strong agreement between the two methods is verified in the previous case (Sect. 3.1). In Figure 10, a comparison between simulated and observed spectral polarimetric variables is presented. The simulations are generated using varying drop wobbling, represented by canting angle distribution widths of  $5^\circ$ ,  $20^\circ$ , and  $30^\circ$ . The maxima and minima for the simulated variables are found to be more pronounced relatively to the measurements. There is sufficient agreement for the first notch of  $s\delta_{HV}$  up to 5 m/s. The simulated  $sZ_{DR}$  exhibits a similar trend to the measurements; however, the amplitude of the maxima is more pronounced, and the minima are significantly deeper. One potential cause of these discrepancies is the assumption that drops have a spheroidal shape (oblate). Therefore, it seems plausible to conclude that the T-matrix approach using spheroids is inadequate to simulate the spectral polarimetric variables of raindrops at higher frequencies, such as 94 GHz. The increasing canting of the drops in simulations (green, orange and blue faint lines in Fig. 10) is causing spectral broadening, that occurs because the wobbling of the drops averages out the distinct polarization signals over a wider range of velocities. The  $sZ_{DR}$  values are spread over a wider range of Doppler

350

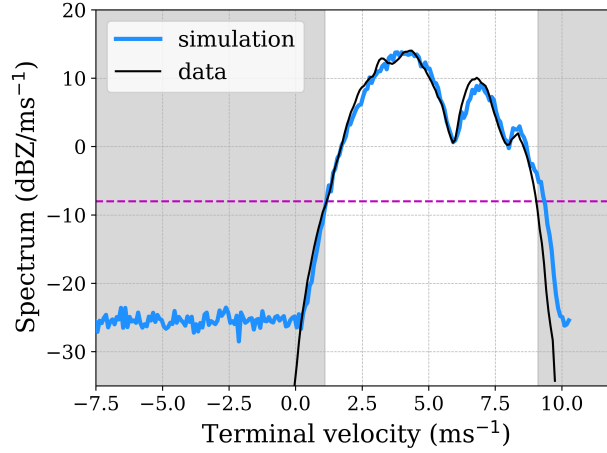


**Figure 9.** 03 February 2021, 12:40 UTC, 484m, Measured Doppler Spectrum (black line) and optimum-fitted Gamma DSD (blue line). The purple dashed line indicates the threshold for applying the Least Squares Method in order to find the optimum fit. The parameters that characterize the fitted spectrum are  $\mu = -0.4$ ,  $D_m = 1.6$  mm,  $N_0 = 688$   $\text{mm}^{-1-\mu} \text{m}^{-3}$ , and  $\sigma_t = 0.15$   $\text{ms}^{-1}$

velocities, reducing the sharpness of the extrema. The more uniform distribution of drop orientations smooths out the  $sZ_{DR}$  signal. Similarly, the broadening of phase differences across the spectrum leads to smeared-out minima and maxima in  $s\delta_{HV}$ , meaning a more gradual and continuous transition in the phase difference between horizontally and vertically polarized waves. In a nutshell, increased canting causes a more isotropic distribution of drop orientations, leading to smoother, less distinct spectral features.

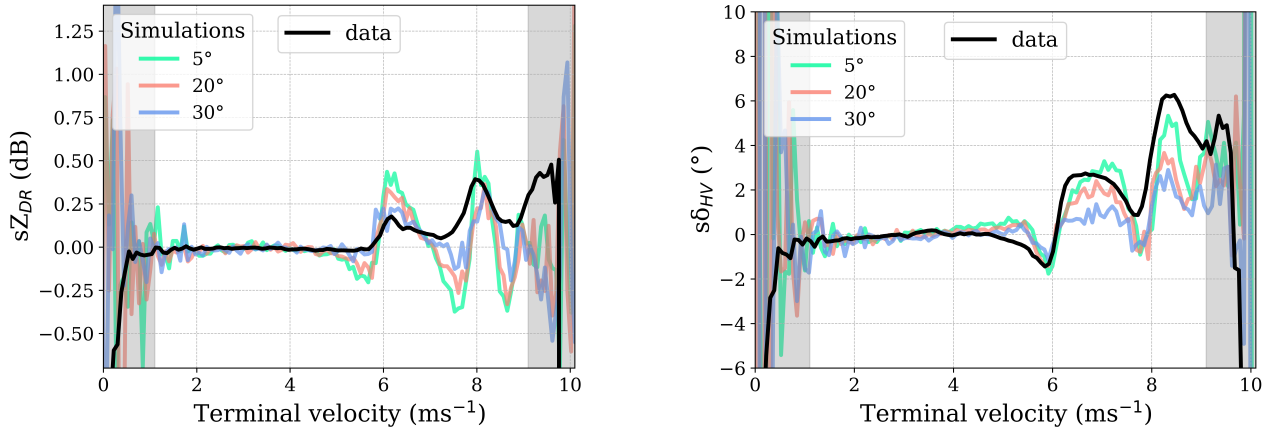


**Figure 10.** Spectral polarimetric variables of case study 2. Left panel: spectral differential reflectivity  $sZ_{DR}$ . Right panel: spectral differential phase  $s\delta_{HV}$ . The black lines represent the measured data, the green, orange and blue faint lines represent the simulations for different canting angle distribution widths (wobbling):  $5^\circ$ ,  $20^\circ$ , and  $30^\circ$  respectively.

## 4 Conclusions and ways forward

In this study, simulations of spectral polarimetric variables were compared with real measurements in rain conditions for different levels of turbulence. The simulation accounts for factors such as the noise present in real measurements, atmospheric turbulence, and the wobbling of raindrops, aiming to replicate the complexities of actual radar data. These effects are considered to ensure a more realistic comparison between the simulated and measured spectral polarimetric variables.

The results reveal that the simulations closely align and show reasonable agreement with observations only within a limited area of the Doppler spectrum, approximately to terminal velocities up to 5 and 7  $ms^{-1}$  (i.e. equi-volume diameters smaller than 1.33 and 2.25 mm), respectively. Overall the position of the notches in the simulations aligns well with the observations, indicating that the velocity distribution and the location of the resonances are properly captured by the simulations. However, the amplitude of the notches is not accurately represented. Notably, the simulations more accurately fit the maxima compared to the minima, especially for the differential phase. The minima in the measured data of both  $sZ_{DR}$  and  $s\delta_{HV}$  appear muted, while the simulated minima are significantly deeper. The maxima and minima differences are stronger in the case of lower turbulence conditions.

These discrepancies pinpoint to potential limitations in the model's treatment of the amplitude modulation caused by scattering. A potential explanation may lie in the assumption used in the T-matrix approach, which models raindrops as spheroids or more generally as rotationally symmetric particles. However raindrops undergo oscillations (Szakáll et al., 2010), thus they may be not characterized by rotational symmetry. This suggests that traditional methods for computing scattering properties such as the well-established T-matrix method may produce inaccurate scattering parameters, especially for resonant particles (i.e. when the radar wavelength becomes comparable or smaller than the raindrop size). Other more accurate methods should be used, e.g. the discrete dipole approximation or method of moments in the surface integral equation approach as proposed in Thurai et al. (2014); Manić et al. (2018). Future work should explore whether such more sophisticated scattering models can indeed explain the observed discrepancies. Otherwise, data acquired in low turbulence conditions can be used to build look-up tables of the polarimetric scattering properties for any given incidence angle in a data-driven approach as recently proposed by Myagkov et al. (2024).

This work paves the way toward using spectral polarimetric observations of millimeter radars for testing scattering computations of rain polarimetric variables. As such it contributes to the broader scientific community's efforts to improve cloud radar simulations, and advance our knowledge of cloud processes and their implications for atmospheric dynamics.

### Code and data availability

The T-matrix code is available at <https://github.com/jleinonen/pytmatrix>. The code for the simulations that include noise and turbulence, as well as the spectra presented in this study will be published at <https://github.com/loanna-Tsik> upon acceptance of the manuscript.


## **Author contribution**

AB conceived the presented idea. AB and IT led the algorithm development, conducted the simulations and analysis. IT drafted the manuscript and designed the figures. CU led the data processing and provided methodological guidance and revisions. EM  
390 contributed with supervision, funding acquisition, project administration and to the overall conceptual framework of the study. All authors edited and reviewed the original draft, provided critical feedback and helped shape the research, analysis and manuscript.

## **Competing interests**

All authors have no competing interests.

## **395 Acknowledgments**

This research has been supported by the PANGEA4CalVal project (Grant Agreement 101079201) funded by the European Union . We also acknowledge the support by the Hellenic Foundation for Research and Innovation (H.F.R.I.) under the “3rd Call for H.F.R.I. Research Projects to support Post-Doctoral Researchers” (Project Acronym: REVEAL, Project Number: 07222). The work by A. Battaglia has been also supported by the European Space Agency under the activities “WInd  
400 VElocity Radar Nephoscope (WIVERN) Phase A Science and Requirements Consolidation Study” (ESA Contract Number RFP/3-18420/24/NL/IB/ab). Finally, this work used instrument and data of the Ruisdael Observatory, a scientific research infrastructure co-financed by the Netherlands Organization for Scientific Research (NWO), grant number 184.034.015. The authors would also like to thank the anonymous referee and Alexander Myagkov for their reviews, which helped improve the paper.

- Andsager, K., Beard, K. V., and Laird, N. F.: Laboratory Measurements of Axis Ratios for Large Raindrops, *Journal of the Atmospheric Sciences*, 56, 2673 – 2683, [https://doi.org/https://doi.org/10.1175/1520-0469\(1999\)056<2673:LMOARF>2.0.CO;2](https://doi.org/https://doi.org/10.1175/1520-0469(1999)056<2673:LMOARF>2.0.CO;2), 1999.
- Atlas, D., Srivastava, R. C., and Sekhon, R. S.: Doppler radar characteristics of precipitation at vertical incidence, *Review of Geophysics*, 11, 1–35, <https://doi.org/10.1029/RG011i001p00001>, 1973.
- 410 Aydin, K. and Lure, Y.-M.: Millimeter wave scattering and propagation in rain: a computational study at 94 and 140 GHz for oblate spheroidal and spherical raindrops, *IEEE Trans. Geosci. Remote Sens.*, 29, 593–601, <https://doi.org/10.1109/36.135821>, 1991.
- Bachmann, S. and Zrníc, D.: Spectral Density of Polarimetric Variables Separating Biological Scatterers in the VAD Display, *J. Atmos. Ocean Technol.*, 24, 1186 – 1198, <https://doi.org/10.1175/JTECH2043.1>, 2007.
- Battaglia, A., Saavedra, P., Rose, T., and Simmer, C.: Characterization of Precipitating Clouds by Ground-Based Measure-  
 415 ments with the Triple-Frequency Polarized Microwave Radiometer ADMIRARI, *J. Appl. Meteorol. Climatol.*, 49, 394 – 414, <https://doi.org/10.1175/2009JAMC2340.1>, 2010.
- Battaglia, A., Martire, P., Caubet, E., Phalippou, L., Stesina, F., Kollias, P., and Illingworth, A.: End to end simulator for the WIVERN W-band Doppler conically scanning spaceborne radar, *Atm. Meas. Tech.*, 2021, 1–31, <https://doi.org/10.5194/amt-2021-342>, 2022.
- Beard, K. V. and Chuang, C.: A New Model for the Equilibrium Shape of Raindrops, *Journal of Atmospheric Sciences*, 44, 1509 – 1524,  
 420 [https://doi.org/https://doi.org/10.1175/1520-0469\(1987\)044<1509:ANMFTE>2.0.CO;2](https://doi.org/https://doi.org/10.1175/1520-0469(1987)044<1509:ANMFTE>2.0.CO;2), 1987.
- Bringi, V. N. and Chandrasekar, V.: *Polarimetric Doppler Weather Radar, Principles and applications*, Cambridge University Press, pp 266, 2001.
- Chandrasekar, V.: Statistical properties of dual-polarized radar signals, *Proc. 23rd on Radar Meteorology, Snowmass*, pp. 192–196, 1986.
- Chandrasekar, V., Beauchamp, R. M., and Bechini, R.: *Introduction to Dual Polarization Weather Radar Introduction to Dual Polarization*  
 425 *Weather Radar Fundamentals, Applications, and Networks*, Cambridge University Press, pp 496, 2023.
- Chen, C., Unal, C. M. H., and Nijhuis, A. C. P. O.: Jensen–Shannon Distance-Based Filter and Unsupervised Evaluation Metrics for Polarimetric Weather Radar Processing, *IEEE Trans. Geosci. Remote Sens.*, 60, 1–18, <https://doi.org/10.1109/TGRS.2022.3200731>, 2022.
- Courtier, B. M., Battaglia, A., Huggard, P. G., Westbrook, C., Mroz, K., Dhillon, R. S., Walden, C. J., Howells, G., Wang, H., Ellison, B. N., Reeves, R., Robertson, D. A., and Wylde, R. J.: First Observations of G-Band Radar Doppler Spectra, *Geophys. Res. Lett.*, 49,  
 430 e2021GL096475, <https://doi.org/https://doi.org/10.1029/2021GL096475>, e2021GL096475 2021GL096475, 2022.
- Courtier, B. M., Battaglia, A., and Mroz, K.: Advantages of G-band radar in multi-frequency, liquid phase microphysical retrievals, *EGU-sphere*, 2024, 1–19, <https://doi.org/10.5194/egusphere-2024-205>, 2024.
- Doviak, R. J. and Zrníc, D. S.: *Doppler Radar and Weather Observations*, Academic Press, 1993.
- Ekelund, R., Eriksson, P., and Kahnert, M.: Microwave single-scattering properties of non-spheroidal raindrops, *Atm. Meas. Tech.*, 13,  
 435 6933–6944, <https://doi.org/10.5194/amt-13-6933-2020>, 2020.
- Frisch, A., Fairall, C., and Snider, J.: Measurement of stratus cloud and drizzle parameters in ASTEX with a K  $\alpha$ -band Doppler radar and a microwave radiometer, *Journal of Atmospheric Sciences*, 52, 2788–2799, 1995.
- Illingworth, A. J., Battaglia, A., Bradford, J., Forsythe, M., Joe, P., Kollias, P., Lean, K., Lori, M., Mahfouf, J.-F., Melo, S., Midthassel, R., Munro, Y., Nicol, J., Potthast, R., Rennie, M., Stein, T. H. M., Tanelli, S., Tridon, F., Walden, C. J., and Wolde, M.: WIVERN: A  
 440 New Satellite Concept to Provide Global In-Cloud Winds, Precipitation, and Cloud Properties, *Bull. Amer. Met. Soc.*, 99, 1669–1687, <https://doi.org/10.1175/BAMS-D-16-0047.1>, 2018.



- Kalesse, H., Szyrmer, W., Kneifel, S., Kollias, P., and Luke, E.: Fingerprints of a riming event on cloud radar Doppler spectra: observations and modeling, *Atmos. Chem. Phys.*, 16, 2997–3012, <https://doi.org/10.5194/acp-16-2997-2016>, 2016.
- Keenan, T. D., Carey, L. D., Zrnić, D. S., and May, P. T.: Sensitivity of 5-cm Wavelength Polarimetric Radar Variables to Raindrop  
445 Axial Ratio and Drop Size Distribution, *Journal of Applied Meteorology*, 40, 526 – 545, [https://doi.org/10.1175/1520-0450\(2001\)040<0526:SOCWPR>2.0.CO;2](https://doi.org/10.1175/1520-0450(2001)040<0526:SOCWPR>2.0.CO;2), 2001.
- Kneifel, S., Kollias, P., Battaglia, A., Leinonen, J., Maahn, M., Kalesse, H., and Tridon, F.: First observations of triple-frequency radar Doppler spectra in snowfall: Interpretation and applications, *Geophys. Res. Lett.*, 43, 2225–2233, <https://doi.org/10.1002/2015GL067618>, 2016.
- 450 Kneifel, S., Leinonen, J., Tyynela, J., Ori, D., and Battaglia, A.: Satellite precipitation measurement, vol. 1 of *Adv. Global Change Res.*, chap. Scattering of Hydrometeors, Springer, ISBN: 978-3-030-24567-2, 2020.
- Kollias, P., Albrecht, B. A., and Marks, F. D.: Raindrop Sorting Induced by Vertical Drafts in Convective Clouds, *Geophys. Res. Lett.*, 28, 2787–2790, 2001.
- Kollias, P., Albrecht, B. A., and Marks, F.: Why Mie? Accurate Observations of Vertical Air Velocities and Raindrops Using a Cloud Radar,  
455 *Bull. Amer. Met. Soc.*, 83, 1471–1483, doi: <http://dx.doi.org/10.1175/BAMS-83-10-1471>, 2002.
- Kollias, P., Rémillard, J., Luke, E., and Szyrmer, W.: Cloud radar Doppler spectra in drizzling stratiform clouds: 1. Forward modeling and remote sensing applications, *Journal of Geophysical Research: Atmospheres*, 116, 2011a.
- Kollias, P., Rémillard, J., Luke, E., and Szyrmer, W.: Cloud radar Doppler spectra in drizzling stratiform clouds: 1. Forward modeling and remote sensing applications, *Journal of Geophysical Research: Atmospheres*, 116, <https://doi.org/10.1029/2010JD015237>,  
460 2011b.
- Kumjian, M. R., Martinkus, C. P., Prat, O. P., Collis, S., van Lier-Walqui, M., and Morrison, H. C.: A Moment-Based Polarimetric Radar Forward Operator for Rain Microphysics, *J. Appl. Meteorol. Climatol.*, 58, 113 – 130, <https://doi.org/10.1175/JAMC-D-18-0121.1>, 2019.
- Lakshmi, A. K. K., Swaroop, S., Biswas, S. K., and Chandrasekar, V.: Study of Microphysical Signatures Based on Spectral Polarimetry during the RELAMPAGO Field Experiment in Argentina, *J. Atmos. Ocean Technol.*, 41, 235 – 260, <https://doi.org/10.1175/JTECH-D-22-0113.1>, 2024.  
465
- Leinonen, J.: High-level interface to T-matrix scattering calculations: architecture, capabilities and limitations, *Opt. Express*, 22, 1655–1660, <https://doi.org/10.1364/OE.22.001655>, 2014.
- Lhermitte, R.: Attenuation and Scattering of Millimeter Wavelength Radiation by Clouds and Precipitation, *Journal of Atmospheric and Oceanic Technology*, 7, 464 – 479, [https://doi.org/10.1175/1520-0426\(1990\)007<0464:AASOMW>2.0.CO;2](https://doi.org/10.1175/1520-0426(1990)007<0464:AASOMW>2.0.CO;2), 1990.
- 470 Li, H. and Moiseev, D.: Melting Layer Attenuation at Ka- and W-Bands as Derived From Multifrequency Radar Doppler Spectra Observations, *J. Geophys. Res. Atm.*, 0, <https://doi.org/10.1029/2019JD030316>, 2019.
- Li, H., Korolev, A., and Moiseev, D.: Supercooled liquid water and secondary ice production in Kelvin–Helmholtz instability as revealed by radar Doppler spectra observations, *Atmos. Chem. Phys.*, 21, 13 593–13 608, <https://doi.org/10.5194/acp-21-13593-2021>, 2021.
- Luke, E. P. and Kollias, P.: Separating Cloud and Drizzle Radar Moments during Precipitation Onset Using Doppler Spectra, *J. Atmos. Ocean Technol.*, 30, 1656 – 1671, <https://doi.org/10.1175/JTECH-D-11-00195.1>, 2013.  
475
- Luke, E. P., Kollias, P., and Shupe, M. D.: Detection of supercooled liquid in mixed-phase clouds using radar Doppler spectra, *J. Geophys. Res. Atm.*, 115, <https://doi.org/10.1029/2009JD012884>, 2010.

Luke, E. P., Yang, F., Kollias, P., Vogelmann, A. M., and Maahn, M.: New insights into ice multiplication using remote-sensing observations of slightly supercooled mixed-phase clouds in the Arctic, *Proceedings of the National Academy of Sciences*, 118, e2021387118, <https://doi.org/10.1073/pnas.2021387118>, 2021.

Mak, H. Y. L. and Unal, C.: Peering into the heart of thunderstorm clouds: insights from cloud radar and spectral polarimetry, *Atmos. Meas. Tech.*, 18, 1209–1242, <https://doi.org/10.5194/amt-18-1209-2025>, 2025.

Manić, S. B., Thurai, M., Brangi, V. N., and Notaroš, B. M.: Scattering Calculations for Asymmetric Raindrops during a Line Convection Event: Comparison with Radar Measurements, *J. Atmos. Ocean Technol.*, 35, 1169 – 1180, <https://doi.org/10.1175/JTECH-D-17-0196.1>, 2018.

Mishchenko, M. I., Hovenier, J. W., and Travis, L. D., eds.: *Light Scattering by Nonspherical Particles*, Academic Press, San Diego, 2000.

Moisseev, D. N. and Chandrasekar, V.: Polarimetric Spectral Filter for Adaptive Clutter and Noise Suppression, *J. Atmos. Ocean Technol.*, 26, 215 – 228, <https://doi.org/10.1175/2008JTECHA1119.1>, 2009.

Moisseev, D. N., Chandrasekar, V., Unal, C. M. H., and Russchenberg, H. W. J.: Dual-Polarization Spectral Analysis for Retrieval of Effective Raindrop Shapes, *J. Atmos. Ocean Technol.*, 23, 1682 – 1695, <https://doi.org/10.1175/JTECH1945.1>, 2006.

Mróz, K., Battaglia, A., Kneifel, S., von Terzi, L., Karrer, M., and Ori, D.: Linking rain into ice microphysics across the melting layer in stratiform rain: a closure study, *Atm. Meas. Tech.*, 14, 511–529, <https://doi.org/10.5194/amt-14-511-2021>, 2021.

Myagkov, A. and Ori, D.: Analytic characterization of random errors in spectral dual-polarized cloud radar observations, *Atmospheric Measurement Techniques*, 15, 1333–1354, <https://doi.org/10.5194/amt-15-1333-2022>, 2022.

Myagkov, A., Kneifel, S., and Rose, T.: Evaluation of the reflectivity calibration of W-band radars based on observations in rain, *Atmospheric Measurement Techniques*, 13, 5799–5825, <https://doi.org/10.5194/amt-13-5799-2020>, 2020.

Myagkov, A., Nomokonova, T., and Frech, M.: Empirical model for backscattering polarimetric variables in rain at W-band: motivation and implications, *Atmospheric Measurement Techniques Discussions*, 2024, 1–30, <https://doi.org/10.5194/amt-2024-143>, 2024.

O'Connor, E. J., Hogan, R. J., and Illingworth, A. J.: Retrieving Stratocumulus Drizzle Parameters Using Doppler Radar and Lidar, *Journal of Applied Meteorology*, 44, 14 – 27, <https://doi.org/10.1175/JAM-2181.1>, 2005.

Pfitzenmaier, L., Unal, C. M. H., Dufournet, Y., and Russchenberg, H. W. J.: Observing ice particle growth along fall streaks in mixed-phase clouds using spectral polarimetric radar data, *Atmos. Chem. Phys.*, 18, 7843–7862, <https://doi.org/10.5194/acp-18-7843-2018>, 2018.

Spek, A. L. J., Unal, C. M. H., Moisseev, D. N., Russchenberg, H. W. J., Chandrasekar, V., and Dufournet, Y.: A New Technique to Categorize and Retrieve the Microphysical Properties of Ice Particles above the Melting Layer Using Radar Dual-Polarization Spectral Analysis, *Journal of Atmospheric and Oceanic Technology*, 25, 482 – 497, <https://doi.org/10.1175/2007JTECHA944.1>, 2008.

Szakáll, M., Mitra, S. K., Diehl, K., and Borrmann, S.: Shapes and oscillations of falling raindrops — A review, *Atmospheric Research*, 97, 416–425, <https://doi.org/10.1016/j.atmosres.2010.03.024>, from the Lab to Models and Global Observations: Hans R. Pruppacher and Cloud Physics, 2010.

Teng, S., Hu, H., Liu, C., Hu, F., Wang, Z., and Yin, Y.: Numerical simulation of raindrop scattering for C-band dual-polarization Doppler weather radar parameters, *J. Quant. Spectrosc. Radiat. Transfer*, 213, 133–142, <https://doi.org/10.1016/j.jqsrt.2018.04.004>, 2018.

Testud, J., Oury, S., Black, R. A., Amayenc, P., and Dou, X.: The Concept of “Normalized” Distribution to Describe Rain-drop Spectra: A Tool for Cloud Physics and Cloud Remote Sensing, *Journal of Applied Meteorology*, 40, 1118 – 1140, [https://doi.org/10.1175/1520-0450\(2001\)040<1118:TCOND>2.0.CO;2](https://doi.org/10.1175/1520-0450(2001)040<1118:TCOND>2.0.CO;2), 2001.

- 515 Thurai, M. and Bringi, V. N.: Drop Axis Ratios from a 2D Video Disdrometer, *Journal of Atmospheric and Oceanic Technology*, 22, 966 – 978, <https://doi.org/10.1175/JTECH1767.1>, 2005.
- Thurai, M., Huang, G. J., Bringi, V. N., Randeu, W. L., and Schönhuber, M.: Drop Shapes, Model Comparisons, and Calculations of Polarimetric Radar Parameters in Rain, *J. Atmos. Ocean Technol.*, 24, 1019 – 1032, <https://doi.org/10.1175/JTECH2051.1>, 2007.
- Thurai, M., Hudak, D., and Bringi, V. N.: On the Possible Use of Copolar Correlation Coefficient for Improving the Drop Size Distribution  
520 Estimates at C Band, *Journal of Atmospheric and Oceanic Technology*, 25, 1873 – 1880, <https://doi.org/10.1175/2008JTECHA1077.1>, 2008.
- Thurai, M., Bringi, V. N., Manić, A. B., Šekeljić, N. J., and Notaroš, B. M.: Investigating raindrop shapes, oscillation modes, and implications for radio wave propagation, *Radio Sci.*, 49, 921–932, <https://doi.org/https://doi.org/10.1002/2014RS005503>, 2014.
- Touzi, R., Lopes, A., Bruniquel, J., and Vachon, P. W.: Coherence estimation for SAR imagery, *IEEE Trans. Geosci. Remote Sens.*, 37,  
525 135–149, 1999.
- Tridon, F. and Battaglia, A.: Dual-frequency radar Doppler spectral retrieval of rain drop size distributions and entangled dynamics variables, *J. Geophys. Res. Atm.*, 120, 5585–5601, <https://doi.org/10.1002/2014JD023023>, 2015.
- Tridon, F., Battaglia, A., and Kollias, P.: Disentangling Mie and attenuation effects in rain using a Ka-W dual-wavelength Doppler spectral ratio technique, *Geophys. Res. Lett.*, 40, 5548–5552, <https://doi.org/10.1002/2013GL057454>, 2013.
- 530 Ulbrich, C. W.: Natural Variations in the Analytical Form of the Raindrop Size Distribution, *Journal of Applied Meteorology and Climatology*, 22, 1764 – 1775, [https://doi.org/https://doi.org/10.1175/1520-0450\(1983\)022<1764:NVITAF>2.0.CO;2](https://doi.org/https://doi.org/10.1175/1520-0450(1983)022<1764:NVITAF>2.0.CO;2), 1983.
- Ulbrich, C. W. and Atlas, D.: Microphysics of Raindrop Size Spectra: Tropical Continental and Maritime Storms, *Journal of Applied Meteorology and Climatology*, 46, 1777 – 1791, <https://doi.org/https://doi.org/10.1175/2007JAMC1649.1>, 2007.
- Unal, C.: Spectral Polarimetric Radar Clutter Suppression to Enhance Atmospheric Echoes, *J. Atmos. Ocean Technol.*, 26, 1781 – 1797,  
535 <https://doi.org/10.1175/2009JTECHA1170.1>, 2009.
- Unal, C.: High-Resolution Raindrop Size Distribution Retrieval Based on the Doppler Spectrum in the Case of Slant Profiling Radar, *J. Atmos. Ocean Technol.*, 32, 1191 – 1208, <https://doi.org/10.1175/JTECH-D-13-00225.1>, 2015.
- Unal, C. and van den Brule, Y.: Exploring Millimeter-Wavelength Radar Capabilities for Raindrop Size Distribution Retrieval: Estimating Mass-Weighted Mean Diameter from the Differential Backscatter Phase, *J. Atmos. Ocean Technol.*, 41, 583 – 603,  
540 <https://doi.org/10.1175/JTECH-D-23-0094.1>, 2024.
- Unal, C. M. H. and Moisseev, D. N.: Combined Doppler and Polarimetric Radar Measurements: Correction for Spectrum Aliasing and Non-simultaneous Polarimetric Measurements, *Journal of Atmospheric and Oceanic Technology*, 21, 443 – 456, [https://doi.org/10.1175/1520-0426\(2004\)021<0443:CDAPRM>2.0.CO;2](https://doi.org/10.1175/1520-0426(2004)021<0443:CDAPRM>2.0.CO;2), 2004.
- Wang, Y., Yu, T.-Y., Ryzhkov, A. V., and Kumjian, M. R.: Application of Spectral Polarimetry to a Hailstorm at Low Elevation Angle, *J. Atmos. Ocean Technol.*, 36, 567 – 583, <https://doi.org/10.1175/JTECH-D-18-0115.1>, 2019.
- 545 Wriedt, T.: Using the T-matrix method for light scattering computations by non-axisymmetric particles: Superellipsoids and realistically shaped particles, *Particle & Particle Systems Characterization: Measurement and Description of Particle Properties and Behavior in Powders and Other Disperse Systems*, 19, 256–268, 2002.
- Yanovsky, F.: Inferring microstructure and turbulence properties in rain through observations and simulations of signal spectra measured with  
550 Doppler–polarimetric radars, in: *Polarimetric Detection, Characterization and Remote Sensing*, edited by Mishchenko, M. I., Yatskiv, Y. S., Rosenbush, V. K., and Videen, G., pp. 501–542, Springer Netherlands, Dordrecht, 2011.

- Yu, T.-Y., Xiao, X., and Wang, Y.: Statistical Quality of Spectral Polarimetric Variables for Weather Radar, *J. Atmos. Ocean Technol.*, 29, 1221 – 1235, <https://doi.org/https://doi.org/10.1175/JTECH-D-11-00090.1>, 2012.
- Zhu, Z., Kollias, P., and Yang, F.: Particle inertial effects on radar Doppler spectra simulation, *Atm. Meas. Tech.*, 16, 3727–3737, <https://doi.org/10.5194/amt-16-3727-2023>, 2023.
- 555 Zrnić, D. S.: Simulation of Weatherlike Doppler Spectra and Signals, *Journal of Applied Meteorology and Climatology*, 14, 619 – 620, [https://doi.org/10.1175/1520-0450\(1975\)014<0619:SOWDSA>2.0.CO;2](https://doi.org/10.1175/1520-0450(1975)014<0619:SOWDSA>2.0.CO;2), 1975.